www.small-methods.com

# Nanoscale Phase and Orientation Mapping in Multiphase Polycrystalline Hafnium Zirconium Oxide Thin Films Using 4D-STEM and Automated Diffraction Indexing

Garrett Baucom, Eitan Hershkovitz, Paul Chojecki, Toshikazu Nishida, Roozbeh Tabrizian, and Honggyu Kim\*

Ferroelectric hafnium zirconium oxide (HZO) holds promise for nextgeneration memory and transistors due to its superior scalability and seamless integration with complementary metal-oxide-semiconductor processing. A major challenge in developing this emerging ferroelectric material is the metastable nature of the non-centrosymmetric polar phase responsible for ferroelectricity, resulting in a coexistence of both polar and non-polar phases with uneven grain sizes and random orientations. Due to the structural similarity between the multiple phases and the nanoscale dimensions of the thin film devices, accurate measurement of phase-specific information remains challenging. Here, the application of 4D scanning transmission electron microscopy is demonstrated with automated electron diffraction pattern indexing to analyze multiphase polycrystalline HZO thin films, enabling the characterization of crystallographic phase and orientation across large working areas on the order of hundreds of nanometers. This approach offers a powerful characterization framework to produce a quantitative and statistically robust analysis of the intricate structure of HZO films by uncovering phase composition, polarization axis alignment, and unique phase distribution within the HZO film. This study introduces a novel approach for analyzing ferroelectric HZO, facilitating reliable characterization of process-structure-property relationships imperative to accelerating the growth optimization, performance, and successful implementation of ferroelectric HZO in devices.

#### 1. Introduction

Ferroelectricity in Si-doped hafnium oxide (HfO<sub>2</sub>) discovered in 2011 has garnered significant interest for its

G. Baucom, E. Hershkovitz, H. Kim
Department of Materials Science and Engineering
University of Florida
Gainesville, FL 32611, USA
E-mail: honggyukim@ufl.edu
P. Chojecki, T. Nishida, R. Tabrizian
Department of Electrical and Computer Engineering
University of Florida
Gainesville, FL 32611, USA

The ORCID identification number(s) for the author(s) of this article can be found under https://doi.org/10.1002/smtd.202400395

DOI: 10.1002/smtd.202400395

potential applications in information storage and processing technologies, such as non-volatile memory devices and field-effect transistors.[1-4] A notable feature of HfO2 is its ability to stabilize regions with spontaneous electric polarization (domains) at nanoscale dimensions. For example, ferroelectricity and electric-field-controlled polarization switching have been demonstrated in HfO2 thin films with thicknesses well below 10 nm with the thinnest reported thickness being a mere 1 nm, offering the exceptional scalability desirable for realizing devices with high density and low power consumption.<sup>[5-8]</sup> This is in stark contrast to conventional ferroelectric materials with a perovskite structure, which suffer from a loss of spontaneous polarization with decreasing size.[9,10] In addition, the thin film growth and processing methods required for building HfO2-based ferroelectric devices are currently employed for conventional semiconductor fabrication and have a low thermal budget, thus offering a straightforward path toward complementary metal-oxidesemiconductor (CMOS) integration of

HfO<sub>2</sub> thin films.<sup>[11,12]</sup> These advantages have spurred the rapid development of a wide range of emerging HfO<sub>2</sub>-based ferroelectric devices, including ferroelectric tunnel junctions, 3D ferroelectric random-access memory, nanoelectromechanical resonators, and ferroelectric analog synaptic transistors.<sup>[4,8,13–18]</sup>

Structurally, HfO<sub>2</sub> is unique in that it can adopt multiple polymorphs. At room temperature and atmospheric pressure, it adopts a monoclinic structure (*m*-phase), which transforms to tetragonal (*t*-phase) and ultimately cubic (*c*-phase) structures with increasing temperature. [19-22] These thermodynamically stable phases are all centrosymmetric and are therefore irresponsible for ferroelectricity. The widely accepted origin of ferroelectricity is a metastable orthorhombic structure (*o*-phase) with space group *Pca2*<sub>1</sub>, which has been thoroughly explored through computational and experimental methods. [19,20,23-25] Extensive research has demonstrated that the ferroelectricity in HfO<sub>2</sub> emerges when HfO<sub>2</sub> thin films are doped with other elements

2366968, D. Downloaded from https://onlinelibtrary.wiely.com/doi/10.1002/smtd.202400395 by Honggyu Kir - University Of Florida, Wiley Online Library on [31/102024]. See the Terms and Conditions (https://onlinelibtrary.wiely.com/terms-and-conditions) on Wiley Online Library for rules of use; OA articles are governed by the applicable Creative Commons License

www.advancedsciencenews.com

CIENCE NEWS

www.small-methods.com

(e.g., Si, Al, Sr) and are geometrically confined (e.g., metalferroelectric-metal structure), followed by a high-temperature annealing process. [26–37] While this approach achieves macroscopic ferroelectricity, challenges persist regarding the mixture of the polar o-phase with non-polar t- and m-phases as well as the random orientation and non-uniform size of the o-phase grains. The ability to produce phase pure thin films with controlled orientation is critical for maximizing device performance metrics such as power consumption and retention in memory devices. The polycrystalline nature and the lack of characterization methods with high spatial resolution and phase sensitivity pose increasing challenges in building robust process-structure-property relationships. Therefore, accurately characterizing the microstructure of ferroelectric thin films such as the phase composition, spatial distribution, and orientation of multiple phases is crucial for understanding the impact of thin film growth parameters on the microstructure of HfO2 thin films and ultimately establishing materials design strategies aimed at achieving targeted performance for relevant devices.

Grazing-incidence x-ray diffraction (GIXRD) is the most common method for the structural characterization of HfO2-based ferroelectric thin films due to its phase sensitivity and nondestructive sample preparation.<sup>[19,38,39]</sup> However, distinguishing the polar o-phase from non-polar phases of fluorite-structured HfO<sub>2</sub> remains challenging due to their similar lattice constants and peak broadening arising from finite size effects, hampering the isolation of diffraction signals from individual phases. [20,21,40] As a result, many x-ray diffraction peaks are labeled as a mixture of multiple phases.[19,39,41,42] Other techniques such as Raman or infrared spectroscopy have also been used in identifying and distinguishing HfO<sub>2</sub> phases.<sup>[43,44]</sup> However, GIXRD, Raman, and infrared spectroscopy are bulk measurements and lack the ability to provide site-specific crystallographic information about the material. Low-energy transmission Kikuchi diffraction (TKD) in scanning electron microscopy (SEM) has been used to reveal the plan-view microstructure of HfO2 thin films, allowing for spatially resolved microstructure analysis.[45-47] However, its spatial resolution is on the order of tens of nanometers, insufficient for ultrathin HfO2 films with nanoscale grains. In addition, the signal from both the top and bottom electrodes partially contributes to the transmitted diffraction patterns, likely degrading the data signal-to-noise ratio. High-angle annular darkfield (HAADF) imaging in conjunction with position averaged convergent beam electron diffraction (PACBED) in scanning transmission electron microscopy (STEM) has been successfully used to identify phase information of individual grains and uncover the structural origin for ferroelectricity in doped HfO<sub>2</sub> thin films.<sup>[48–51]</sup> However, such atomic-scale structure information is available only for grains whose major zone axes align close to the observation direction in STEM, limiting the statistical analysis of the microstructure. More recently, scanning based electron diffraction techniques in STEM have been employed to characterize grain size distributions and reveal the phase and orientation information of individual grains in fluorite-structured oxide thin films.[52-55] While these studies hold promise in the highresolution microstructural analysis of thin films, the information is restricted to either a limited range of orientations or a few specific polymorphs. Therefore, there is a pressing need to develop a methodology that enables unambiguous determination

of both phase and orientation information of individual grains in HfO<sub>2</sub> thin films featuring multiple phases, non-uniform grain size, and random orientation.

Here, we demonstrate high-resolution phase and orientation mapping of multiphase polycrystalline hafnium zirconium oxide (Hf<sub>0.5</sub>Zr<sub>0.5</sub>O<sub>2</sub>, HZO) thin films using 4DSTEM. This technique generates a 4D dataset consisting of 2D diffraction patterns captured at every position of the electron probe scanned over a 2D region within the specimen. Utilizing an automated diffraction pattern indexing technique established in this work, we reveal the spatial distribution of grains with both polar and non-polar phases, providing the phase and orientation information of a 10 nm-thick polycrystalline HZO film with a spatial resolution of ≈1.5 nm. The resulting phase and orientation maps are further confirmed and validated using HAADF and annular bright-field (ABF)-STEM imaging. Our approach enables a quantitative analysis of the HZO microstructure such as phase compositions and preferred alignment of the polarization axis of polar phase grains. This comprehensive microstructure analysis with high spatial resolution over a large field of view (500 nm wide) highlights the ability to conduct robust statistical analysis of the complex structure of HZO thin films, crucial for understanding the effectiveness of thin film growth controls and establishing thin film growth and processing strategies toward predictable and controllable microstructure and ferroelectric performance.

#### 2. Results and Discussion

#### 2.1. Automated Diffraction Indexing Method

We used a TiN-HZO-TiN heterostructure as a model system, relevant to ferroelectric random access memory devices and ferroelectric tunnel junctions, to perform the microstructure analysis of HZO thin films. The metal-ferroelectric-metal (MFM) structure was subject to a cyclic application of electric fields (i.e., wake-up cycling), exhibiting a single-loop hysteresis in the polarization and voltage curve (Figure S1, Supporting Information) which is the characteristic feature of ferroelectric materials. The low-magnification HAADF-STEM image in Figure 1a shows the cross-section view of the MFM structure consisting of a 10 nmthick HZO thin film confined by 10 nm-thick TiN electrodes as well as the top Pt layer. To characterize the phase and orientation of individual grains within the HZO thin film, 4D-STEM was employed to collect spatially resolved electron diffraction patterns across the MFM structure. Figure 1b shows the schematic of the 4D-STEM data acquisition using an electron microscope pixel array detector (EMPAD).[56] In this work, we acquired a series of nanobeam electron diffraction (NBED) patterns in 4D-STEM using a near-parallel electron probe with the semi-convergence angle of ≈0.9 mrad. As a result, each NBED pattern displays a collection of well-separated diffraction spots whose geometric positions and intensities offer crystal structure and orientation information. 4D-STEM data was collected from the red dotted box area (500 nm  $\times$  26 nm) in Figure 1a that covers the MFM structure. The electron probe with a diameter of ≈1.5 nm full-width halfmaximum (Figure S2, Supporting Information) was employed to secure high spatial resolution and cover the local area larger than the projected unit cell sizes of all the reported polymorphs.

www.advancedsciencenews.com

www.small-methods.com

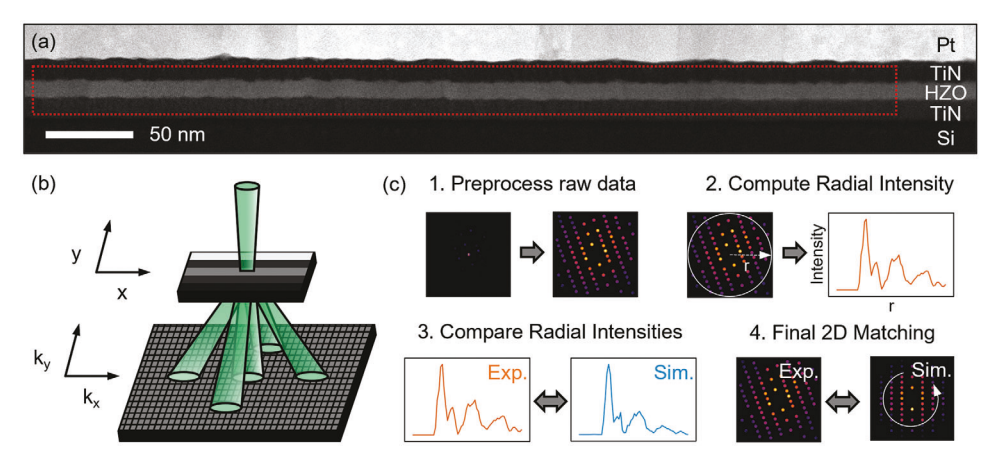


Figure 1. a) HAADF-STEM image showing the structure of the MFM device; the area of the sample scanned with 4D-STEM is indicated by the red dotted rectangle. b) Schematic of the 4D-STEM acquisition and c) the pattern matching procedure used in this study. The procedure starts with preprocessing raw data from the detector and simulations, and then a radially integrated intensity profile is calculated for each image. The profiles of the experimental and simulation patterns are compared using cross-correlation to narrow the number of patterns to finally compare directly, accounting for rotation to find the single best match.

Thus, the resultant NBED patterns are representative of the local crystal structure.

Figure 1c illustrates the procedure of the automated diffraction indexing process. To determine the phase and orientation information from the 4D-STEM dataset, each experimental NBED pattern is compared with dynamic electron diffraction simulation data for the reported polymorphs along all possible orientations. To determine which phases to perform electron diffraction simulation for, we used GIXRD to identify possible phases that may be present in our sample. The GIXRD spectrum (Figure S3, Supporting Information) shows strong reflections at  $2\theta$  values associated with m-phase (space group  $P2_1/c$ ), t-phase (space group P42/nmc), and o-phase (space group Pca21). We note that reflections associated with the polar rhombohedral phase (space group R3m<sup>[57,58]</sup> are not observed in our sample. Matching each experimental NBED pattern with a large volume of simulation data (> 10<sup>4</sup> unique patterns) using an exhaustive search is computationally slow. To address this, we utilized the radially integrated 1D diffraction intensity profiles to create a screened group of the most similar simulated NBED patterns using normalized cross-correlation (NCC). Then, the best match from the screened group was ultimately determined by performing NCC between the 2D simulated and experimental NBED patterns with the consideration of the in-plane rotation of NBED patterns. This significantly accelerated the computational process by reducing the number of 2D image comparisons needed. As the grain size in HZO thin films is on the order of tens of nanometers, we prepared a thin TEM lamella with a thickness of ≈8 nm to mitigate the occurrence of multiple grains within a single diffraction pattern caused by overlap along the viewing direction. The bestmatched simulation data for individual NBED patterns in the 4D-STEM dataset offers the phase identity and orientation information, resulting in corresponding 2D maps across the films over a relatively large working area that are discussed in the following section. The NBED simulation parameters (Table S1, Supporting Information), matching procedure, and preprocessing of the data (Figure S4, Supporting Information) are further discussed in detail in the Supporting Information.

#### 2.2. Phase and Orientation Maps

Figure 2a,b displays the phase map and corresponding orientation maps of the *m*-, *o*-, and *t*-phases. The phase map in Figure 2a shows that the dominant phase present is the polar o-phase, as expected from the measured hysteresis loop in Figure S1 (Supporting Information). The phase fraction of the o-phase is 52% while those of the non-polar m- and t-phases are 11% and 37%, respectively. While macroscopic ferroelectricity was measured in the HZO thin film after the high-temperature heat treatment and wake-up cycling, a large fraction of the film remained non-polar. The coexistence of both polar and non-polar phases observed in this work is consistent with previous experimental studies on HZO thin films grown with similar growth methods and processing conditions (e.g., atomic layer deposition, confined geometry, and high-temperature annealing). [16,59] The orientation maps for the three HZO phases are shown in Figure 2b, providing the spatial distribution of each phase with the in-plane orientation information along the viewing direction in STEM.

To evaluate the reliability of our analysis, we inspected both the experimental and matching simulated NBED patterns from several well-defined grains. Representative diffraction patterns from three areas in the *o*-phase are shown in **Figure 3b**. Excellent agreement is found between the experimental diffraction patterns and the matched simulated patterns. Comparisons between experimental and matching simulated NBED patterns from the *m*-and *t*-phases are shown in Figure S5 (Supporting Information). Among the three areas examined in the *o*-phase region, Area 2 is close to a low-index zone axis, that is, [010], thus we performed atomic-resolution STEM imaging to further confirm the correctness of our measurements.

Figure 4a,b displays HAADF and ABF images that show the arrangement of constituent atoms. HAADF imaging provides an image contrast that depends on the atomic number.<sup>[60]</sup> Due to the low atomic number of oxygens, only cation (Hf/Zr) atomic columns are visible in Figure 4a. On the other hand, ABF imaging enables simultaneous visualization of heavy and light elements, in which atomic columns appear as dark contrast.<sup>[61–65]</sup>

23669608, 0, Downloaded from https://onlinelibrary.wiley.com/doi/10.1002/smtd.202400395 by Honggyu Kim - University Of Florida , Wiley Online Library on [31/10/2024]. See the Terms and Conditions (https://onlinelibrary.wiley.com/doi/10.1002/smtd.202400395 by Honggyu Kim - University Of Florida , Wiley Online Library on [31/10/2024]. See the Terms and Conditions (https://onlinelibrary.wiley.com/doi/10.1002/smtd.202400395 by Honggyu Kim - University Of Florida , Wiley Online Library on [31/10/2024]. See the Terms and Conditions (https://onlinelibrary.wiley.com/doi/10.1002/smtd.202400395 by Honggyu Kim - University Of Florida , Wiley Online Library on [31/10/2024]. See the Terms and Conditions (https://onlinelibrary.wiley.com/doi/10.1002/smtd.202400395 by Honggyu Kim - University Of Florida , Wiley Online Library on [31/10/2024]. See the Terms and Conditions (https://onlinelibrary.wiley.com/doi/10.1002/smtd.202400395 by Honggyu Kim - University Of Florida , Wiley Online Library on [31/10/2024]. See the Terms and Conditions (https://onlinelibrary.wiley.com/doi/10.1002/smtd.202400395 by Honggyu Kim - University Of Florida , Wiley Online Library on [31/10/2024]. See the Terms and Conditions (https://onlinelibrary.wiley.com/doi/10.1002/smtd.202400395 by Honggyu Kim - University Of Florida , Wiley Online Library on [31/10/2024].

ons) on Wiley Online Library for rules of use; OA articles are governed by the applicable Creative Commons

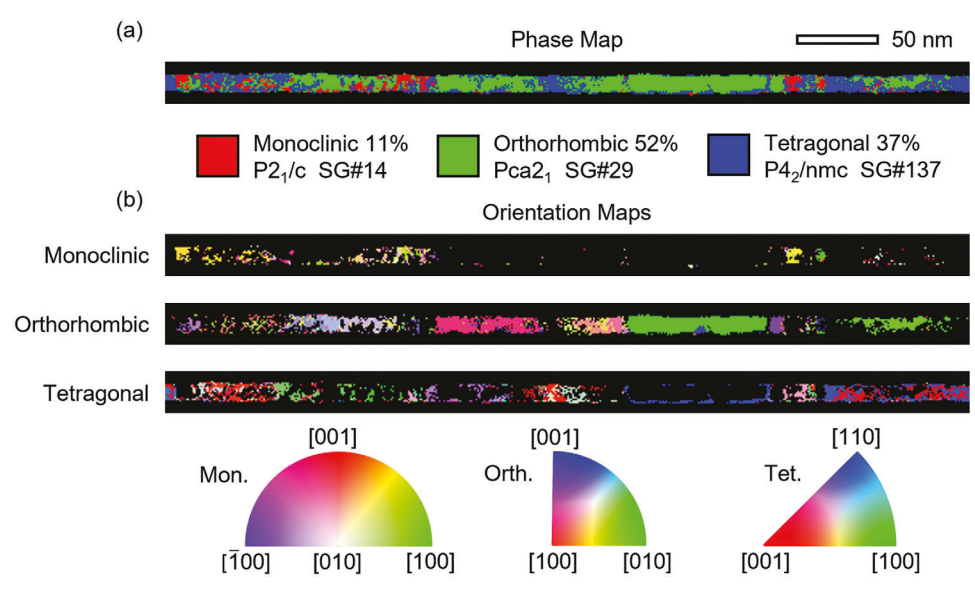


Figure 2. a) Phase map of the HZO layer, showing the dominance of the o-phase phase, with residual m- and t-phase. b) Determined in-plane (zone-axis) orientation maps for each phase.

Both cation and anion atomic columns revealed in HAADF and ABF images are matched with the [010] projection of the ophase, confirming the 4D-STEM analysis results in Figure 2. In Figure 4b, the Hf/Zr atomic columns are the darkest, while the O columns appear lighter. We note that Areas 1 and

3 represent grains highly tilted from major zone axes, thus atomic-resolution HAADF and/or ABF images are not available. However, the unique geometry and intensity of diffraction spots enable the phase and orientation determination for both grains, demonstrating the phase and orientation analysis

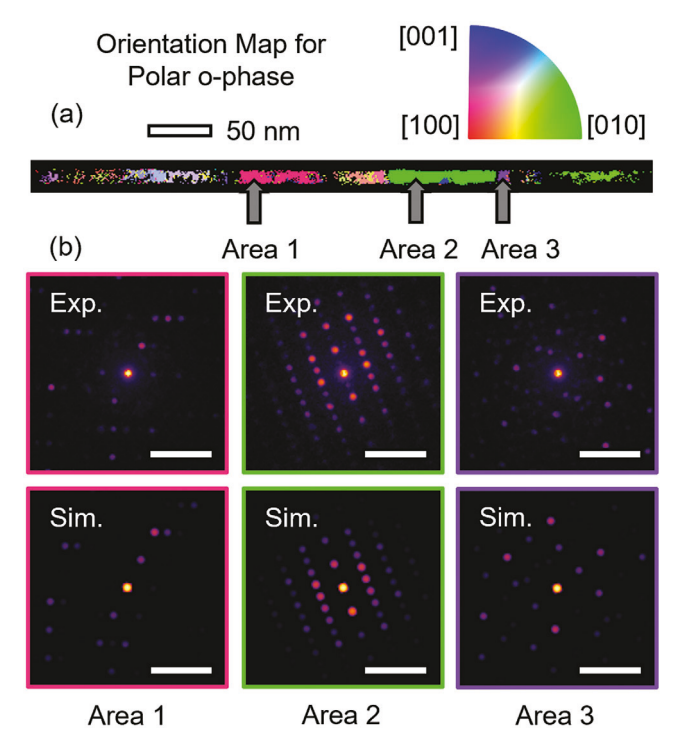


Figure 3. a) Orientation map of the o-phase. b) Experimental diffraction patterns from the areas indicated by the arrows in (a) with the best-matched simulation pattern given below. Scale bars in (b) indicate 1 Å-1.

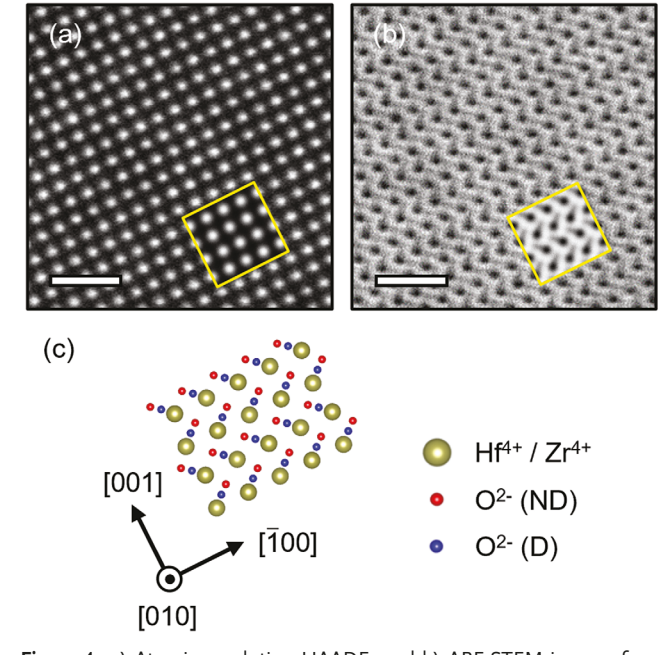
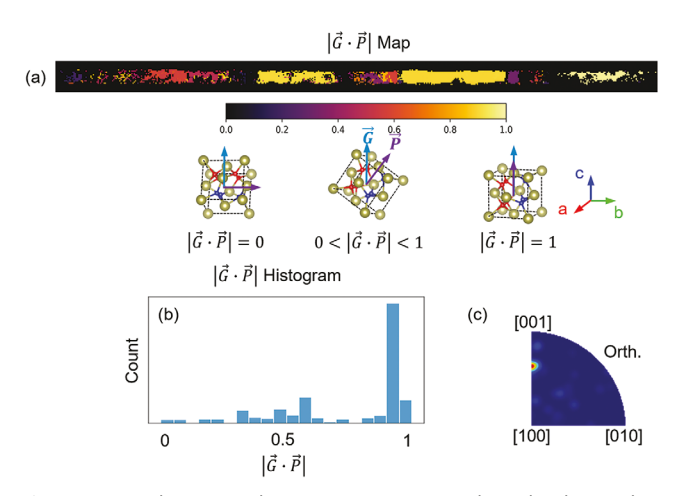


Figure 4. a) Atomic resolution HAADF- and b) ABF-STEM images from the region identified by the arrow in Figure 3 as Area 2. Scale bars indicate 1 nm. Yellow boxed regions are simulated STEM images, which show agreement with the experimental images. c) Schematic of HZO corresponding to the region in (a,b) marked with the yellow dotted box. ND denotes an oxygen atom that is not displaced during polarization switching while D indicates an atom that is displaced.

www.advancedsciencenews.com

www.small-methods.com



**Figure 5.** a) Polarization alignment map computed via the dot product showing how well the o-phase grains are aligned with the [001] polarization axis. b) Histogram of the polarization alignments showing strong alignment with [001], with a small secondary distribution of alignments  $\approx$ 60 degrees from [001]. c) Inverse pole figure showing the out-of-plane texture of the o-phase.

of multiphase polycrystalline materials which is critical for HZO research.

#### 2.3. Orientation of Polar Axis

The orientation of the polarization axis within the o-phase grain is an important structural property relevant to ferroelectric performance. Recently, Lee et al. reported a detailed analysis of the effects of crystallographic orientation on the ferroelectric properties of HZO and revealed a drastic difference in polarization switching and domain dynamics between (111) and (001) textured HZO films. [66] This result along with previous studies focusing on the microstructure texture in HfO2-based ferroelectrics highlights the importance of comprehensive characterization of the HZO crystallographic microstructure. [67–70]

Here, we present a statistical analysis of the orientation of the polarization axis in the polar o-phase grains. 2D electron diffraction patterns provide crystallographic orientation information along the viewing direction and normal to the viewing direction. Here, we define the crystal orientation along the growth direction (vertically normal to the viewing direction) as the vector G and the polarization axis in the HfO2 system (the [001] direction) as the vector P. Then, we calculate the dot product of G and P to inspect how the polarization axis is aligned within the MFM structure. Because the polarization direction is switchable, we are interested only in the magnitude of this dot product, not the sign. Figure 5a shows the map of the magnitude of this dot product ranging from 0 to 1, representing an alignment of the polarization axis perpendicular or parallel to the growth direction, respectively. While the in-plane orientation of the polar o-phase seems random in Figure 2b, the statistical analysis of the dot product and the corresponding inverse pole figure in Figure 5b,c reveals that a large volume of the o-phase in this region is aligned close to the [102] direction, ≈26 degrees from the [001] direction. We performed the same analysis for two additional areas in the film, which show similar agreement with

this area (Figure S6, Supporting Information). Previous studies report that the microstructure of HZO films can be influenced by the texture of the electrodes. [53,66,71] The analysis of the TiN electrodes in this film using 4D-STEM shows that the electrodes are not strongly textured, so there is no obvious effect of the texture of the electrode on the HZO film (Figures S7 and S8, Supporting Information). This result suggests that the preferential orientation in the HZO film is not controlled only by the electrode texture, but rather that control of thin film growth and post-growth processing parameters may also serve as a means to manipulate the orientation of the polar *o*-phase grains within HZO films.

#### 2.4. Domain Structure and Phase Distribution

As demonstrated above, the combination of 4D-STEM and automated diffraction indexing facilitates the analysis of microstructures in HZO films. This includes determining the phase fraction and alignment of the polarization axis within the polar ophase, offering insights into the formation of multiple metastable phases. Furthermore, utilizing cross-section imaging with a nano-sized electron probe enables the characterization of the local domain structure and phase distribution across the MFM structure.

First, using our approach, we determined the presence of 90° domain walls within a polar o-phase grain, a feature previously identified in Gd-doped HfO2 via HAADF-STEM imaging.[72] In the orientation map of the polar o-phase (Figure 6a), the red box highlights a small region oriented along [001] (blue), within a relatively large o-phase grain oriented along [010] (green), indicating the presence of a 90° domain wall. To corroborate this information, we collected HAADF images displayed in Figure 6b. The yellow dotted lines indicate the location of the domain boundary detected by the automated indexing method. The magnified HAADF image from the [010]-oriented region (green dotted box in Figure 6b) is displayed in Figure 6c. Correspondingly, the image from the [001]-oriented region (blue dotted box in Figure 6b) is displayed in Figure 6d. The arrangement of the cations (Hf/Zr) exhibits a notable difference. Specifically, in the [010] projection, four adjacent cations form a parallelogram, while in the [001] projection, they appear as a trapezoid. These unique cation atomic arrangements agree with the atomic models along both projections as depicted in Figure 6e.

Another notable feature revealed by our analysis is the formation of the *t*-phase near the interface between the HZO film and electrode. Shown in **Figure 7a** is the magnified portion of the phase map where the *t*-phase exists between the *o*-phase and the bottom TiN electrode. Figure 7b,c shows representative NBED patterns from the *o*- and *t*-phase, respectively, with the corresponding simulated NBED patterns below (Figure 7e,f). Additionally, the experimental and simulated NBED patterns for the TiN electrode directly below this area are given in Figure 7d,g. We observed that the [110] projection of the *t*-phase is aligned with the [010] projection of the *o*-phase while the (\bar{1}10) plane of the *t*-phase is parallel with the (001) plane of the *o*-phase. We note that there are extra diffraction spots found in the experimental *t*-phase NBED pattern (white arrows in Figure 7c) that are not seen in the simulated NBED pattern (Figure 7f). Due to the finite

23669608, 0, Downloaded from https://onlinelibrary.wiley.com/doi/10.1002/smtd.202400395 by Honggyu Kim - University Of Florida , Wiley Online Library on [31/10/2024]. See the Terms and Conditions (https://onlinelibrary.wiley

onditions) on Wiley Online Library for rules of use; OA articles are governed by the applicable Creative Commons

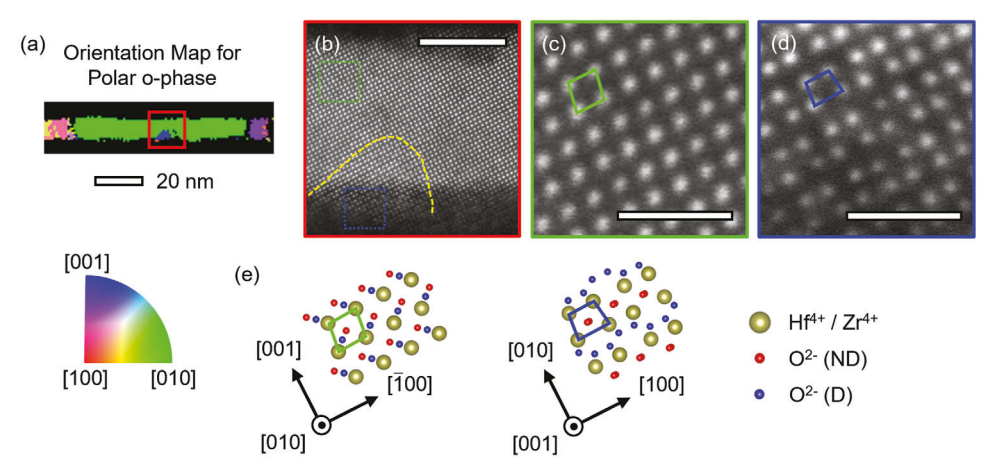
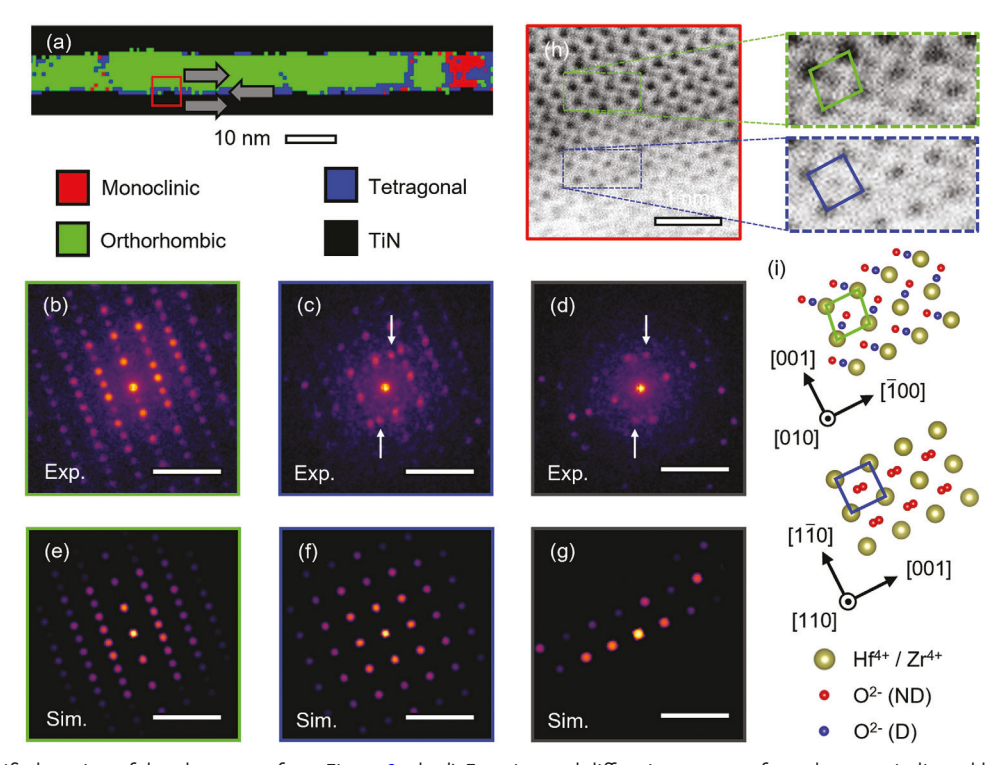


Figure 6. a) Orientation map of the o-phase. b) HAADF-STEM image showing the existence of 90° domain boundaries (dashed yellow line) within an o-phase grain. c) Magnified HAADF-STEM image of an o-phase [010] region (green dotted box in a). d) Magnified HAADF-STEM image of an o-phase [001] region (blue dotted box in a). e) Atomic model of o-phase [010] (left) and [001] (right). ND denotes an oxygen atom that is not displaced during polarization switching while D indicates an atom that is displaced. The difference in Hf/Zr atom arrangement between the two orientations is highlighted with a parallelogram and trapezoid. Scale bar in (b) indicates 5 nm and scale bars in (c,d) indicate 1 nm.

size of the electron probe ( $\approx$ 1.5 nm) and the *t*-phase formed in proximity to the bottom electrode, the extra peaks arise from the diffraction signal from TiN (white arrows in Figure 7d). Figure 7h highlights the transition from *o*-phase to *t*-phase at the bottom electrode interface with an ABF-STEM image. The atomic ar-

rangements revealed by the image show excellent agreement with the projected structures of *ο*-phase [010] and *t*-phase [110] given in Figure 7i, with the atomic arrangements of the Hf/Zr columns changing from a parallelogram to a square arrangement. Additionally, STEM multislice simulations (Figure S9,



**Figure 7.** a) Magnified portion of the phase map from Figure 2a. b–d) Experimental diffraction patterns from the areas indicated by the grey arrows in (a). The white arrows in (c,d) indicate diffraction spots that arise from overlap with the TiN electrode. e–g) Simulated diffraction patterns of o-phase [010], t-phase [110], and TiN matching the patterns shown in (b–d). h) ABF-STEM image of the interface between t-phase and o-phase taken from the area indicated by the red box in (a). The boxed green and blue regions highlight the o-phase and t-phase, respectively. i) Atomic models of o-phase [010] (top) and t-phase [110] (bottom). ND denotes an oxygen atom that is not displaced during polarization switching while D indicates an atom that is displaced. The difference in Hf/Zr atom arrangement between the two orientations is highlighted with a parallelogram and square. Scale bars in (b–g) indicate 1 Å $^{-1}$ .

23669608, 0, Downloaded from https://onlinelibrary.wiley.com/doi/10.1002/smtd.202400395 by Honggyu Kim - University Of Florida , Wiley Online Library on [31/10/2024]. See the Terms and Conditions (https://onlinelibrary.wiley.com/term

and-conditions) on Wiley Online Library for rules of use; OA articles are governed by the applicable Creative Commons

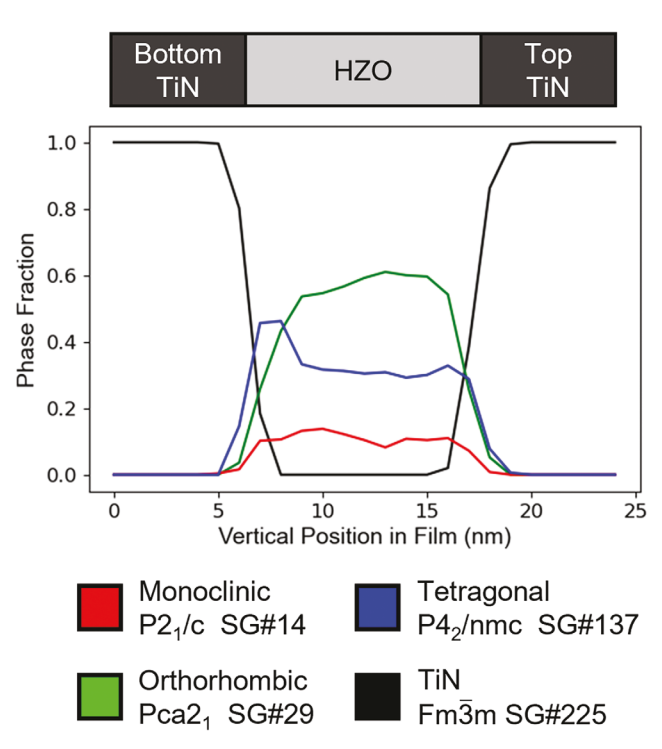
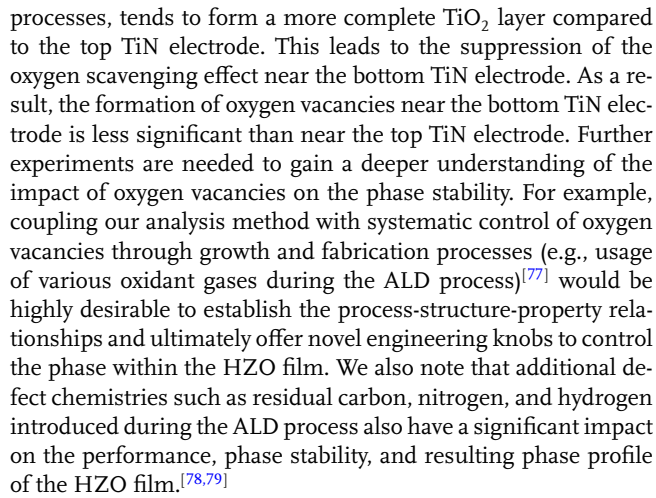


Figure 8. Phase composition profiles across the TiN-HZO-TiN structure.

Supporting Information) show excellent agreement with our experimental STEM images in both the Hf/Zr columns and the O columns.

The t-phase formation at local regions, identified above, motivated us to inspect the spatial distribution of polar and nonpolar phases across the MFM structure over a large field of view. Figure 8 displays the phase composition profile along the growth direction constructed using the phase map in Figure 2a. The t-phase exhibits peak concentration adjacent to the bottom electrode while the o-phase shows high concentrations throughout the HZO film. It is widely accepted that oxygen vacancies play a critical role in stabilizing the t- and o-phases over the mphase.<sup>[73–75]</sup> Due to the oxygen scavenging characteristic of Ti in the TiN electrode, oxygen vacancies preferentially form near the interface between the HZO and TiN electrode.<sup>[75]</sup> This suggests that the t-phase near the interface is likely associated with oxygen vacancy generation during the film deposition and rapid thermal annealing process. Analyzing the phase profile in Figure 8, we also observed an asymmetric t-phase distribution, indicating that the bottom interface is a favored site for *t*-phase formation. Additionally, mild asymmetry was observed in the o-phase profile, with a lower o-phase concentration near the bottom interface compared to the top interface. We performed a similar phase analysis for different areas within the same MFM sample (Figure \$10, Supporting Information), showing a consistent result featuring asymmetric phase profiles for the t- and o-phases. We note that the asymmetry in the phase profile can be linked with the asymmetry in oxidation conditions for the top and bottom TiN electrodes.<sup>[76]</sup> Specifically, the bottom TiN electrode, exposed to the atmosphere after its growth when using a sputter and an oxygen-rich environment during atomic layer deposition (ALD)



Lastly, the stabilization of the *t*-phase at the interfaces can be linked with the suppression of ferroelectric behaviors of thin HZO films. Walters et al.<sup>[77]</sup> observed a significant reduction and even absence of switched polarization – the polarization relevant for memory applications – as the thickness of HZO films decreases, even following wake-up cycling. They attributed this phenomenon to the presence of the *t*-phase within the HZO films, evidenced by slight shifts and broadening of diffraction peaks in GIXRD patterns. The phase profile analysis presented in Figure 8 delineates the specific location of the *t*-phase, not just locally but across a relatively large area (>10,000 nm²). This result underscores the necessity for site-specific strategies during thin film growth to stabilize the polar *o*-phase and enhance ferroelectricity in ultrathin films.

#### 3. Conclusion

We have demonstrated the characterization of phase and crystallographic orientation for multiple polar and non-polar phases in ferroelectric HZO utilizing 4D-STEM and automated diffraction indexing. This approach provides detailed phase and orientation mapping with near-unit-cell spatial resolution and sub-micron field-of-view allowing for quantitative, site-specific characterization of phase information (i.e., phase composition, alignment of the polar axis, and phase/domain boundaries) of multiphase polycrystalline HZO films. Our results exemplify this novel characterization method as a powerful tool for investigating and isolating the effects of individual growth, fabrication, and design parameters in HZO. Furthermore, the success of our method with polycrystalline HZO showcases its capability for being utilized in other complex material systems where new functionalities stem from the phase metastability and nanoscale competition of multiple phases. The findings from this method show great potential to support novel nanoscale microstructure engineering routes for HfO<sub>2</sub>-based ferroelectrics aiming for improved, controllable, and predictable performance. Lastly, we emphasize that the characterization framework established here can be readily coupled with in situ experiments (e.g., heating and/or biasing) in STEM, enabling precise characterization of the dynamic behaviors of multiple phases in HZO films, critical to understanding the cyclic performance of ferroelectric HZO films (e.g., wake-up effect, imprint, and fatigue).

www.small-methods.com

# 4. Experimental Section

www.advancedsciencenews.com

Sample Growth Methods: The TiN - HZO - TiN capacitors were deposited on p+ silicon substrates by ALD using a Cambridge Nano Fiji ALD reactor. The 10 nm TiN layers were deposited by alternating tetrakis(dimethylamido) titanium(IV) and N2 plasma, and the 10 nm HZO layer was deposited using tetrakis (dimethylamido) hafnium (IV) and tetrakis (dimethylamido) zirconium (IV) precursors that were each oxidized using a sequential O2, H2 plasma process as described in the previous study.[77] 50 nm thick Pt top electrodes were then deposited via sputtering. Finally, rapid thermal annealing (RTA) was performed at 500 °C for  $20 \text{ s in N}_2$ .

Sample Preparation and STEM Imaging: Cross sectional TEM samples of the HZO thin films were prepared using a FEI Helios G4 PFIB CXe Dual Beam FIB/SEM. Final cleaning cycle of the TEM specimens was conducted using Xe ions at 5 kV. STEM imaging was performed using a Themis Z (Thermo Fisher) C<sub>s</sub> probe corrected microscope with an acceleration voltage of 200 kV and a probe semi convergence angle of 22 mrad. HAADFand ABF-STEM imaging was performed with a 50-200 mrad and 12-23 mrad collection angle, respectively. 4D-STEM acquisitions were conducted at 200 kV with an electron probe semi-convergence angle of 0.9 mrad and a full-width at half-maximum probe size of ≈1.5 nm (Figure S2, Supporting Information). The electron probe was measured using an FEI CETA 16 bit CMOS camera. The electron probe was formed in uProbe mode using a 50 µm C2 condenser aperture. The electron diffraction patterns were recorded using an electron microscope pixel array detector (EMPAD) with a dwell time of 10 ms. [56] A camera length of 580 mm was chosen for clear separation of adjacent diffraction spots while still capturing many weak high-order reflections. Each scan region was 500 nm × 40 nm with  $500 \times 40$  scan points, which was cropped to  $500 \times 26$  in post-processing to exclude the sample outside of the MFM structure. The sample thickness was measured by acquiring position averaged convergent beam electron diffraction (PACBED) patterns from the Si substrate directly below the HZO film stack with an FEI CETA 16 bit CMOS camera. [80] Comparison with simulated PACBED patterns of varying thickness (Figure S11, Supporting Information) generated using the multislice method indicated a sample thickness of  $\approx 8$  nm. [80,81]

Diffraction Pattern Simulations: The simulation library of electron diffraction patterns used for matching with 4D-STEM data was constructed using computationally determined structural information given for pure-phase HfO<sub>2</sub>.<sup>[24]</sup> The atomic structure of the mixed-phase  $Hf_xZr_{1-x}O_2$  is not often explored via computational methods, but due to the physical and chemical similarity of Hf and Zr, it is reasonable to consider HZO to be similar enough to pure-phase HfO2 or ZrO2. The most experimentally observed phases were simulated, the *m*-, *o*-, and *t*-phases. In other implementations of 4D-STEM orientation mapping algorithms, simple kinematic diffraction simulations are usually used for comparison with experimental data.[82-85] For orientation determination of simple systems, such as cubic silicon, using kinematic simulations is more than sufficient for the complexity of the given problem. However, the HZO system is more complex and requires a precise and clear distinction between very similar structures. Some diffraction patterns from similar phases in HZO possess similar spot positions but differ in intensity due to multiple scattering effects. As such, the effects of multiple scattering were considered in these simulations to achieve more accurate simulations by using dynamical diffraction simulations based on the Bloch wave method. [86] In this work, a library of 18,500 total diffraction patterns was used covering the full range of unique crystallographic directions in the most experimentally observed m-, o-, t-phases for HZO as well as the cubic TiN. Detailed information about the simulations is given in Table S1 (Supporting Information).

Multislice STEM Simulations: The abTEM Python package[87] was utilized to create the ABF and HAADF-STEM multislice simulations shown in Figure 4 and Figure S9 (Supporting Information). The structure files used were the same as those used for the Bloch wave diffraction simulations, pure-phase HfO<sub>2</sub> from a computational study.<sup>[24]</sup> A total supercell thickness of 8 nm was chosen to match the thickness provided by this PACBED analysis (Figure S11, Supporting Information). Shot noise was simulated with Poisson noise corresponding to an electron dose of  $10^6 \, e^- \, \mathring{A}^{-2}$  and to approximate the effect of source size, a 0.4 Å standard deviation Gaussian filter was applied to the final image.

## **Supporting Information**

Supporting Information is available from the Wiley Online Library or from the author.

## Acknowledgements

G.B. and E.H. contributed equally to this work. This work was supported by the U.S. National Science Foundation CAREER program (Grant no. DMR 2338558). The microscopy work was supported by the Research Opportunity Seed Fund (ROSF) from the University of Florida. The authors acknowledge the Research Service Centers at the Herbert Wertheim College of Engineering at the University of Florida. E.H. and P.C. acknowledge the University of Florida Graduate School Fellowship.

#### **Conflict of Interest**

The authors declare no conflict of interest.

## **Data Availability Statement**

The data that support the findings of this study are available from the corresponding author upon reasonable request.

## Keywords

4D-STEM, ferroelectrics, hafnium zirconium oxide, microstructure, nanobeam electron diffraction, phase metastability

> Received: March 18, 2024 Revised: May 1, 2024 Published online:

- [1] T. S. Böscke, J. Müller, D. Bräuhaus, U. Schröder, U. Böttger, Appl. Phys. Lett. 2011, 99, 102903.
- [2] M. H. Park, Y. H. Lee, H. J. Kim, Y. J. Kim, T. Moon, K. D. Kim, J. Müller, A. Kersch, U. Schroeder, T. Mikolajick, C. S. Hwang, Adv. Mater. 2015, 27. 1811.
- [3] J. Müller, T. S. Böscke, U. Schröder, S. Mueller, D. Bräuhaus, U. Böttger, L. Frey, T. Mikolajick, Nano Lett. 2012, 12, 4318.
- [4] J. Müller, T. S. Böscke, D. Bräuhaus, U. Schröder, U. Böttger, J. Sundqvist, P. Kücher, T. Mikolajick, L. Frey, Appl. Phys. Lett. 2011, 99, 112901
- [5] S. S. Cheema, D. Kwon, N. Shanker, R. dos Reis, S.-L. Hsu, J. Xiao, H. Zhang, R. Wagner, A. Datar, M. R. McCarter, C. R. Serrao, A. K. Yadav, G. Karbasian, C.-H. Hsu, A. J. Tan, L.-C. Wang, V. Thakare, X. Zhang, A. Mehta, E. Karapetrova, R. V. Chopdekar, P. Shafer, E. Arenholz, C. Hu, R. Proksch, R. Ramesh, J. Ciston, S. Salahuddin, Nature 2020, 580, 478,
- [6] S. J. Kim, J. Mohan, H. S. Kim, J. Lee, C. D. Young, L. Colombo, S. R. Summerfelt, T. San, J. Kim, Appl. Phys. Lett. 2018, 113, 182903.
- [7] X. Tian, S. Shibayama, T. Nishimura, T. Yajima, S. Migita, A. Toriumi, Appl. Phys. Lett. 2018, 112, 102902.

www.small-methods.com

www.advancedsciencenews.com

- [8] S. S. Cheema, N. Shanker, C.-H. Hsu, A. Datar, J. Bae, D. Kwon, S. Salahuddin, Adv. Electronic Mater. 2022, 8, 2100499.
- [9] J. Celinska, V. Joshi, S. Narayan, L. McMillan, C. Paz de Araujo, Appl. Phys. Lett. 2003, 82, 3937.
- [10] J. F. Ihlefeld, D. T. Harris, R. Keech, J. L. Jones, J.-P. Maria, S. Trolier-McKinstry, J. Am. Ceram. Soc. 2016, 99, 2537.
- [11] S. J. Kim, D. Narayan, J.-G. Lee, J. Mohan, J. S. Lee, J. Lee, H. S. Kim, Y.-C. Byun, A. T. Lucero, C. D. Young, S. R. Summerfelt, T. San, L. Colombo, J. Kim, Appl. Phys. Lett. 2017, 111, 242901.
- [12] S. J. Kim, J. Mohan, J. Lee, J. S. Lee, A. T. Lucero, C. D. Young, L. Colombo, S. R. Summerfelt, T. San, J. Kim, Appl. Phys. Lett. 2018, 112, 172902.
- [13] Y. Arimoto, H. Ishiwara, MRS Bulletin 2004, 29, 823.
- [14] D. Panda, T.-Y. Tseng, Thin Solid Films 2013, 531, 1.
- [15] M. H. Park, Y. H. Lee, T. Mikolajick, U. Schroeder, C. S. Hwang, MRS Commun. 2018, 8, 795.
- [16] A. I. Khan, A. Keshavarzi, S. Datta, Nat. Electron 2020, 3, 588.
- [17] M. Seo, M.-H. Kang, S.-B. Jeon, H. Bae, J. Hur, B. C. Jang, S. Yun, S. Cho, W.-K. Kim, M.-S. Kim, K.-M. Hwang, S. Hong, S.-Y. Choi, Y.-K. Choi, IEEE Electron Device Lett. 2018, 39, 1445.
- [18] T. Tharpe, E. Hershkovitz, F. Hakim, H. Kim, R. Tabrizian, *Nat. Electron* 2023, 6, 599.
- [19] A. Kersch, R. Ganser, M. Trien, Front. Nanotechnol. 2022, 4, 1026286.
- [20] L. Azevedo Antunes, R. Ganser, C. Kuenneth, A. Kersch, Phys. Stat. Sol. (RRL) – Rapid Res. Lett. 2022, 16, 2100636.
- [21] A. Kersch, M. Falkowski, physica status solidi (RRL) Rapid Res. Lett. 2021, 15, 2100074.
- [22] O. Ohtaka, H. Fukui, T. Kunisada, T. Fujisawa, K. Funakoshi, W. Utsumi, T. Irifune, K. Kuroda, T. Kikegawa, J. Am. Ceram. Soc. 2001, 84, 1369.
- [23] X. Sang, E. D. Grimley, T. Schenk, U. Schroeder, J. M. LeBeau, Appl. Phys. Lett. 2015, 106, 162905.
- [24] R. Materlik, C. Künneth, A. Kersch, J. Appl. Phys. 2015, 117, 134109.
- [25] H. Du, C. Groh, C.-L. Jia, T. Ohlerth, R. E. Dunin-Borkowski, U. Simon, J. Mayer, *Matter* 2021, 4, 986.
- [26] D. H. Triyoso, P. J. Tobin, B. E. White, R. Gregory, X. D. Wang, Appl. Phys. Lett. 2006, 89, 132903.
- [27] M. Hyuk Park, H. Joon Kim, Y. Jin Kim, W. Lee, T. Moon, C. Seong Hwang, Appl. Phys. Lett. 2013, 102, 242905.
- [28] P. D. Lomenzo, Q. Takmeel, C. Zhou, C. M. Fancher, E. Lambers, N. G. Rudawski, J. L. Jones, S. Moghaddam, T. Nishida, J. Appl. Phys. 2015, 117, 134105.
- [29] M. H. Park, H. J. Kim, Y. J. Kim, Y. H. Lee, T. Moon, K. D. Kim, S. D. Hyun, C. S. Hwang, Appl. Phys. Lett. 2015, 107, 192907.
- [30] D. Zhou, J. Xu, Q. Li, Y. Guan, F. Cao, X. Dong, J. Müller, T. Schenk, U. Schröder, Appl. Phys. Lett. 2013, 103, 192904.
- [31] G. Walters, A. Shekhawat, N. G. Rudawski, S. Moghaddam, T. Nishida, Appl. Phys. Lett. 2018, 112, 192901.
- [32] M. Hyuk Park, H. Joon Kim, Y. Jin Kim, T. Moon, C. Seong Hwang, Appl. Phys. Lett. 2014, 104, 072901.
- [33] H. J. Kim, M. H. Park, Y. J. Kim, Y. H. Lee, W. Jeon, T. Gwon, T. Moon, K. D. Kim, C. S. Hwang, Appl. Phys. Lett. 2014, 105, 192903.
- [34] P. D. Lomenzo, P. Zhao, Q. Takmeel, S. Moghaddam, T. Nishida, M. Nelson, C. M. Fancher, E. D. Grimley, X. Sang, J. M. LeBeau, J. L. Jones, J. Vac. Sci. Technol. B 2014, 32, 03D123.
- [35] A. Shekhawat, G. Walters, C.-C. Chung, R. Garcia, Y. Liu, J. Jones, T. Nishida, S. Moghaddam, ECS J. Solid State Sci. Technol. 2020, 9, 024011.
- [36] A. Shekhawat, G. Walters, C.-C. Chung, R. Garcia, Y. Liu, J. Jones, T. Nishida, S. Moghaddam, *Thin Solid Films* 2019, 677, 142.
- [37] P. D. Lomenzo, Q. Takmeel, S. Moghaddam, T. Nishida, Thin Solid Films 2016, 615, 139.
- [38] Y. Oh, H.-B. Kim, S. W. Lee, M. J. Jeong, T. J. Park, J.-H. Ahn, Ceram. Int. 2022, 48, 25661.

- [39] M. H. Park, T. Schenk, C. M. Fancher, E. D. Grimley, C. Zhou, C. Richter, J. M. LeBeau, J. L. Jones, T. Mikolajick, U. Schroeder, J. Mater. Chem. C 2017, 5, 4677.
- [40] L. Azevedo Antunes, R. Ganser, R. Alcala, T. Mikolajick, U. Schroeder, A. Kersch, Appl. Phys. Lett. 2021, 119, 082903.
- [41] K. P. Kelley, A. N. Morozovska, E. A. Eliseev, Y. Liu, S. S. Fields, S. T. Jaszewski, T. Mimura, S. Calderon, E. C. Dickey, J. F. Ihlefeld, S. V. Kalinin, *Nat. Mater.* 2023, 22, 1144.
- [42] R. Han, P. Hong, B. Zhang, M. Bai, J. Hou, J. Yang, W. Xiong, S. Yang, J. Gao, Y. Lu, F. Liu, F. Luo, Z. Huo, J. Appl. Phys. 2023, 134, 194104.
- [43] S. Fan, S. Singh, X. Xu, K. Park, Y. Qi, S. W. Cheong, D. Vanderbilt, K. M. Rabe, J. L. Musfeldt, npj Quantum Mater. 2022, 7, 32.
- [44] U. Schroeder, R. Sachdeva, P. D. Lomenzo, B. Xu, M. Materano, T. Mikolajick, A. Kersch, J. Appl. Phys. 2022, 132, 214104.
- [45] M. Lederer, P. Bagul, D. Lehninger, K. Mertens, A. Reck, R. Olivo, T. Kämpfe, K. Seidel, L. M. Eng, ACS Appl. Electron. Mater. 2021, 3, 4115.
- [46] M. Lederer, A. Reck, K. Mertens, R. Olivo, P. Bagul, A. Kia, B. Volkmann, T. Kämpfe, K. Seidel, L. M. Eng, Appl. Phys. Lett. 2021, 118, 012901.
- [47] M. Lederer, T. Kämpfe, R. Olivo, D. Lehninger, C. Mart, S. Kirbach, T. Ali, P. Polakowski, L. Roy, K. Seidel, Appl. Phys. Lett. 2019, 115, 222902.
- [48] Q. Luo, Y. Cheng, J. Yang, R. Cao, H. Ma, Y. Yang, R. Huang, W. Wei, Y. Zheng, T. Gong, J. Yu, X. Xu, P. Yuan, X. Li, L. Tai, H. Yu, D. Shang, Q. Liu, B. Yu, Q. Ren, H. Lv, M. Liu, Nat. Commun. 2020, 11, 1391.
- [49] S. Zhang, Q. Zhang, F. Meng, T. Lin, B. Zeng, L. Gu, M. Liao, Y. Zhou, Research 2023, 6, 0093.
- [50] L. Bégon-Lours, M. Mulder, P. Nukala, S. de Graaf, Y. A. Birkhölzer, B. Kooi, B. Noheda, G. Koster, G. Rijnders, *Phys. Rev. Mater.* 2020, 4, 043401.
- [51] X. Li, H. Zhong, T. Lin, F. Meng, A. Gao, Z. Liu, D. Su, K. Jin, C. Ge, Q. Zhang, L. Gu, Adv. Mater. 2023, 35, 2207736.
- [52] Y.-H. Kim, S.-H. Yang, M. Jeong, M.-H. Jung, D. Yang, H. Lee, T. Moon, J. Heo, H. Y. Jeong, E. Lee, Y.-M. Kim, Small 2022, 18, 2107620.
- [53] K. Chae, S. F. Lombardo, N. Tasneem, M. Tian, H. Kumarasubramanian, J. Hur, W. Chern, S. Yu, C. Richter, P. D. Lomenzo, M. Hoffmann, U. Schroeder, D. Triyoso, S. Consiglio, K. Tapily, R. Clark, G. Leusink, N. Bassiri-Gharb, P. Bandaru, J. Ravichandran, A. Kummel, K. Cho, J. Kacher, A. I. Khan, ACS Appl. Mater. Interfaces 2022, 14, 36771.
- [54] K. Taki, N. Sekine, K. Watanabe, Y. Miyatake, T. Akazawa, H. Sakumoto, K. Toprasertpong, S. Takagi, M. Takenaka, *Nature Comms*. 2024, 15, 3549.
- [55] T.-J. Chang, H.-Y. Chen, C.-I. Wang, H.-C. Lin, C.-F. Hsu, J.-F. Wang, C.-H. Nien, C.-S. Chang, I. P. Radu, M.-J. Chen, *Acta Materialia* 2023, 246, 118707.
- [56] M. W. Tate, P. Purohit, D. Chamberlain, K. X. Nguyen, R. Hovden, C. S. Chang, P. Deb, E. Turgut, J. T. Heron, D. G. Schlom, D. C. Ralph, G. D. Fuchs, K. S. Shanks, H. T. Philipp, D. A. Muller, S. M. Gruner, *Microscopy Microanalys.* 2016, 22, 237.
- [57] K. Liu, F. Jin, X. Zhang, K. Liu, Z. Zhang, E. Hua, J. Zhang, H. Ye, G. Gao, C. Ma, L. Wang, W. Wu, Adv. Funct. Mater. 2023, 33, 2209925.
- [58] Y. Wei, P. Nukala, M. Salverda, S. Matzen, H. J. Zhao, J. Momand, A. S. Everhardt, G. Agnus, G. R. Blake, P. Lecoeur, B. J. Kooi, J. Íñiguez, B. Dkhil, B. Noheda, *Nature Mater* 2018, 17, 1095.
- [59] Y. Lee, Y. Goh, J. Hwang, D. Das, S. Jeon, *IEEE Trans. Electron Devices* 2021, 68, 523.
- [60] S. J. Pennycook, D. E. Jesson, Ultramicroscopy 1991, 37, 14.
- [61] S. D. Findlay, T. Saito, N. Shibata, Y. Sato, J. Matsuda, K. Asano, E. Akiba, T. Hirayama, Y. Ikuhara, Appl. Phys. Express 2010, 3, 116603.
- [62] R. Ishikawa, E. Okunishi, H. Sawada, Y. Kondo, F. Hosokawa, E. Abe, Nat. Mater. 2011, 10, 278.
- [63] S. D. Findlay, N. Shibata, H. Sawada, E. Okunishi, Y. Kondo, T. Yamamoto, Y. Ikuhara, Appl. Phys. Lett. 2009, 95, 191913.

www.advancedsciencenews.com

SCIENCE NEWS

www.small-methods.com

- [64] S. D. Findlay, N. Shibata, H. Sawada, E. Okunishi, Y. Kondo, Y. Ikuhara, Ultramicroscopy 2010, 110, 903.
- [65] E. Okunishi, H. Sawada, Y. Kondo, Micron 2012, 43, 538.
- [66] Y. Lee, R. A. Broughton, H. A. Hsain, S. K. Song, P. G. Edgington, M. D. Horgan, A. Dowden, A. Bednar, D. H. Lee, G. N. Parsons, M. H. Park, J. L. Jones, J. Appl. Phys. 2022, 132, 244103.
- [67] M. Hyuk Park, H. Joon Kim, Y. Jin Kim, T. Moon, C. Seong Hwang, Appl. Phys. Lett. 2014, 104, 072901.
- [68] Z. Fan, J. Deng, J. Wang, Z. Liu, P. Yang, J. Xiao, X. Yan, Z. Dong, J. Wang, J. Chen, Appl. Phys. Lett. 2016, 108, 012906.
- [69] J. Lyu, I. Fina, R. Bachelet, G. Saint-Girons, S. Estandía, J. Gázquez, J. Fontcuberta, F. Sánchez, Appl. Phys. Lett. 2019, 114, 222901.
- [70] K.-W. Huang, S.-H. Yi, Y.-S. Jiang, W.-C. Kao, Y.-T. Yin, D. Beck, V. Korolkov, R. Proksch, J. Shieh, M.-J. Chen, *Acta Materialia* 2021, 205, 116536.
- [71] S. F. Lombardo, M. Tian, K. Chae, J. Hur, N. Tasneem, S. Yu, K. Cho, A. C. Kummel, J. Kacher, A. I. Khan, Appl. Phys. Lett. 2021, 119, 092901.
- [72] E. D. Grimley, T. Schenk, T. Mikolajick, U. Schroeder, J. M. LeBeau, Adv. Mater. Interfaces 2018, 5, 1701258.
- [73] L. Azevedo Antunes, R. Ganser, U. Schroeder, T. Mikolajick, A. Kersch, Adv. Mater. Interfaces 2024, 11, 2300710.
- [74] J. Lee, K. Yang, J. Y. Kwon, J. E. Kim, D. I. Han, D. H. Lee, J. H. Yoon, M. H. Park, Nano Convergence 2023, 10, 55.
- [75] N. Tasneem, H. Kashyap, K. Chae, C. Park, P. Lee, S. F. Lombardo, N. Afroze, M. Tian, H. Kumarasubramanian, J. Hur, H. Chen, W. Chern, S. Yu, P. Bandaru, J. Ravichandran, K. Cho, J. Kacher, A. C. Kummel, A. I. Khan, ACS Appl. Mater. Interfaces 2022, 14, 43897.
- [76] R. Alcala, M. Materano, P. D. Lomenzo, P. Vishnumurthy, W. Hamouda, C. Dubourdieu, A. Kersch, N. Barrett, T. Mikolajick, U. Schroeder, Adv. Funct. Mater. 2023, 33, 2303261.

- [77] G. Walters, A. Shekhawat, S. Moghaddam, J. L. Jones, T. Nishida, Appl. Phys. Lett. 2020, 116, 032901.
- [78] M. H. Park, D. H. Lee, K. Yang, J.-Y. Park, G. T. Yu, H. W. Park, M. Materano, T. Mittmann, P. D. Lomenzo, T. Mikolajick, U. Schroeder, C. S. Hwang, J. Mater. Chem. C 2020, 8, 10526.
- [79] H.-S. Jung, S. H. Jeon, H. K. Kim, I.-H. Yu, S. Y. Lee, J. Lee, Y. J. Chung, D.-Y. Cho, N.-I. Lee, T. J. Park, J.-H. Choi, S. Han, C. S. Hwang, ECS J. Solid State Sci. Technol. 2012, 1, N33.
- [80] J. M. LeBeau, S. D. Findlay, L. J. Allen, S. Stemmer, Ultramicroscopy 2010, 110, 118.
- [81] E. J. Kirkland, Advanced Computing in Electron Microscopy, Springer International Publishing, Cham 2020.
- [82] B. H. Savitzky, S. E. Zeltmann, L. A. Hughes, H. G. Brown, S. Zhao, P. M. Pelz, T. C. Pekin, E. S. Barnard, J. Donohue, L. Rangel DaCosta, E. Kennedy, Y. Xie, M. T. Janish, M. M. Schneider, P. Herring, C. Gopal, A. Anapolsky, R. Dhall, K. C. Bustillo, P. Ercius, M. C. Scott, J. Ciston, A. M. Minor, C. Ophus, *Microsc. Microanalys.* 2021, 27, 712.
- [83] C. Ophus, S. E. Zeltmann, A. Bruefach, A. Rakowski, B. H. Savitzky, A. M. Minor, M. C. Scott, Microsc. Microanalys. 2022, 28, 390.
- [84] N. Cautaerts, P. Crout, H. W. Ånes, E. Prestat, J. Jeong, G. Dehm, C. H. Liebscher, *Ultramicroscopy* 2022, 237, 113517.
- [85] D. Viladot, M. Véron, M. Gemmi, F. Peiró, J. Portillo, S. Estradé, J. Mendoza, N. Llorca-Isern, S. Nicolopoulos, *Journal of Microscopy* 2013, 252, 23.
- [86] J. Spence, J.-M. Zuo, Electron Microdiffraction, Springer International Publishing, Berlin, Germany 1992.
- [87] J. Madsen, T. Susi, Open Research Europe 2021, 1, 24.